Physica B 697 (2025) 416735

Contents lists available at ScienceDirect

Physica B: Condensed Matter

journal homepage: www.elsevier.com/locate/physb

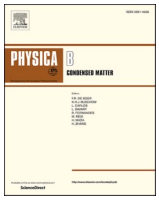

The effect of guanidinium tetrafluoroborate surface passivation on the stability of 2D-PEA_2SnI_4 perovskite thin films prepared by sequential physical vapor deposition

Alex Sembito [a,b], Julius M. Mwabora [a], Francis W. Nyongesa [a], Mmantsae Diale [b,*]

[a] University of Nairobi, P.O. Box 30197-00100, Nairobi, Kenya
[b] University of Pretoria, Private Bag X20, Hatfield, 0028, South Africa

ARTICLE INFO

Keywords:
Guanidinium tetrafluoroborate
Physical vapor deposition
Surface treatment
Film stability
Perovskites

ABSTRACT

2D-PEA_2SnI_4 perovskites thin films were prepared by sequential physical vapor deposition (SPVD), and passivated in vacuum using guanidinium tetrafluoroborate ($GuaBF_4$). The effect of $GuaBF_4$ on stability, optical, morphological, electrical, and structural properties of PEA_2SnI_4 films was investigated. The introduction of $GuaBF_4$ improved the film morphology and crystallinity with the resulting films exhibiting enlarged grain sizes and low surface roughness. Raman and FTIR results showed that $GuaBF_4$ did not change the structural phase and the functional group of the perovskite, but rather confirmed an additive-perovskite interaction. PL and carrier lifetime measurements revealed a 1.8 and 2-folds increment in intensity and lifetime respectively, attributed to suppression of non-radiative recombination in $GuaBF_4$ treated films. XRD, UV–Vis and FE-SEM stability studies showed that $GuaBF_4$ treatment significantly improved the stability of the films. This study suggests an effective strategy for deposition of solvent-free additive based 2D-Sn perovskite high quality films that are stable and reproducible.

1. Introduction

Organic-inorganic hybrid perovskite (OIHP) materials have recently attracted much attention for applications in optoelectronics [1–3]. This has been attributed to their excellent optoelectronic properties and cost effective fabrication techniques [4,5]. However, there are critical issues surrounding the rapidly developing 3D Pb-based perovskite devices ranging from toxicity to environmental instability. These challenges need to be addressed for implementation of such perovskites on an industrial scale. On the other hand, 2D perovskites consist of long chain spacer cations which do not only improve their thermal and moisture stability; but also suppress ion migration making them promising candidates for electronic device applications [6–8]. Ruddlesden-Popper (RP) perovskite phase is one of the mostly studied 2D perovskites due its interesting properties which include high exciton binding energy, composition-dependent photoluminescence (PL), and stability [9]. These perovskites are of the form A_2BX_4, where A is a long organic spacer cation such as phenethylammonium (PEA^+), butylammonium (BA^+) or fluorophenethylammonium ($FPEA^+$), B represents divalent metal cations such as Pb^{2+} or Sn^{2+}, and X represents halide anions such as chloride (Cl^-), bromide (Br^-), or iodide (I^-).

Studies have demonstrated that 2D Sn-based perovskites have a potential of replacing the toxic 2D Pb-based perovskite materials for optoelectronics [10]. Moreover Sn-based perovskites have comparable or better optoelectronic properties than their Pb-based counterparts [11]. However, there is still a big performance gap between the Sn and Pb-perovskite optoelectronic devices with the former still lagging behind. The easy oxidation of Sn^{2+} to Sn^{4+} still remains a challenge for Sn-based perovskites as it leads to films with high Sn^{2+} vacancy defect densities [12,13]. In addition, Sn perovskites tend to crystallize rapidly compared to their Pb-based perovskite counterparts resulting in poor film coverage and morphology [14].

The use of functional molecular additives has been one of the strategies employed to address these challenges. These include reducing agents [15–18], passivators [19–22], solvents [1], or spacer cations [23]. For example, Yuan et al. introduced valeric acid (VA) into PEA_2SnI_4 perovskite precursor to suppress Sn^{2+} oxidation and improve on the film quality. Due to VA and Sn^{2+} strong coordination, perovskite crystallization was better controlled, resulting in good film morphology [22].

* Corresponding author.
E-mail address: mmantsae.diale@up.ac.za (M. Diale).

https://doi.org/10.1016/j.physb.2024.416735
Received 5 August 2024; Received in revised form 25 October 2024; Accepted 11 November 2024
Available online 12 November 2024

Notably, additives composed of the guanidinium cation ($CH_6N_3^+$, Gua^+) and tetrafluoroborate anion (BF_4^-) have recently gained much attention for applications in 3D Pb-based perovskites. Gua^+ consists of a highly symmetric structure whereas the BF_4^-'s ionic radius and chemical properties are comparable to that of the iodide anion. Such properties have been found to improve the morphological and optoelectronic properties of perovskites resulting in better perovskite solar cell performance [24,25]. Some of the Gua^+ based additives used in perovskites include; guanidinium thiocyanate (GuaSCN) [26,27], guanidinium iodide (GuaI) [28,29], guanidinium bromide (GuaBr) [30,31], guanidinium lead trichloride ($GuaPbCl_3$) [32], and guanidinium chloride (GuaCl) [33]. On the other hand, BF_4^- containing compounds used in perovskites include potassium tetrafluoroborate (KBF_4) [24] and imidazolium tetrafluoroborate (IMBF4) [34]. For example, Yu et al. employed KBF_4 to modulate the phase distribution in a quasi 2D-perovskite [24]. It was observed that BF_4^- suppressed the formation of small n domains and passivated the surface halide anion vacancies. Kim et al. used imidazolium tetrafluoroborate ($IMBF_4$) in a mixed Pb-Sn 3D-perovskite [34]. The IM^+ and BF_4^- helped to passivate the defects and improved crystallinity of the films, with the resulting perovskite solar cell exhibiting a power conversion efficiency (PCE) of over 19 %.

Hence in regards to the above, exploiting the synergistic effects of Gua^+ and BF_4^-, is likely to greatly improve the film quality and passivation of defects resulting in suppression of non-radiative charge carrier recombination. According to our literature survey, we note that Gua^+ and BF_4^- containing additives have been majorly limited to 3D Pb-based perovskites with solution processing being the dormant method of application. We therefore extend the application of Gua^+ and BF_4^- containing additive via physical vapor surface treatment to 2D Sn-based perovskites synthesized by sequential physical vapor deposition (SPVD). It is further noted that while solution processed additive-based 2D-Sn perovskites have been widely reported, there are few reports on application of additives via vacuum deposition techniques. Growth of additive-based perovskites using vacuum deposition offers several advantages such as elimination of the use of toxic solvents, reproducibility, and control over film quality and thickness [35].

In this work, 2D- PEA_2SnI_4 perovskites thin films were grown by SPVD and passivated by physical vapor surface treatment using $GuaBF_4$ making the whole deposition process solvent-free. The films were synthesized by first depositing 50 nm SnI_2 followed by 100 nm PEAI. The resulting annealed films were then surface passivated by thermally evaporating different thicknesses of $GuaBF_4$ (0.5, 1 and 1.5 nm). The effect of $GuaBF_4$ surface treatment on the stability, morphological, structural, optical and electrical properties of 2D-PEA_2SnI_4 films was then investigated. $GuaBF_4$ passivated the grain boundaries and surface defects of the 2D Sn-based perovskite resulting in better film morphology and suppressed non-radiative recombination. Additionally, the strong coordination between BF_4^- and Sn^{2+} resulted in enhanced stability of the films. This study suggests a feasible way of depositing solvent-free, stable, and high quality 2D Sn-based perovskite thin films.

2. Experimental

Materials: SnI_2 (99.999 %), SnO_2 (99.9 %), and PEAI (98 %) were acquired from Sigma Aldrich. $GuaBF_4$ and $PC_{70}BM$ (95 %) were obtained from GreatCell Solar Materials and Ossila respectively. All chemicals were used as received without any further purification.

Substrate cleaning: FTO glass substrates with dimensions of about 15 × 20 mm were ultrasonicated using a detergent, acetone, isopropanol, and deionized water sequentially for 20 min each. After drying with nitrogen gas, the substrates were UV/ozone cleaned for 20 min.

PEA_2SnI_4 perovskite film deposition: The schematic for the growth and surface treatment process of 2D-PEA_2SnI_4 perovskite thin films by SPVD is depicted in Fig. 1. Extran solution was used to clean the glass dome of the resistive evaporator to remove any possible contaminants. Clean FTO glass substrates were mounted above the boron nitride crucibles A_1 and A_2 at the same level as the quartz crystal monitor and thermocouple which was used to monitor the film thickness and substrate temperature respectively. Boron nitride crucibles A_1 and A_2 were loaded with SnI_2 and PEAI precursors respectively followed by evacuation of the chamber to a pressure of 2×10^{-5} mbar. 50 nm SnI_2 and 100 nm PEAI were sequentially evaporated at an average rate of 0.3 and 1 Å/

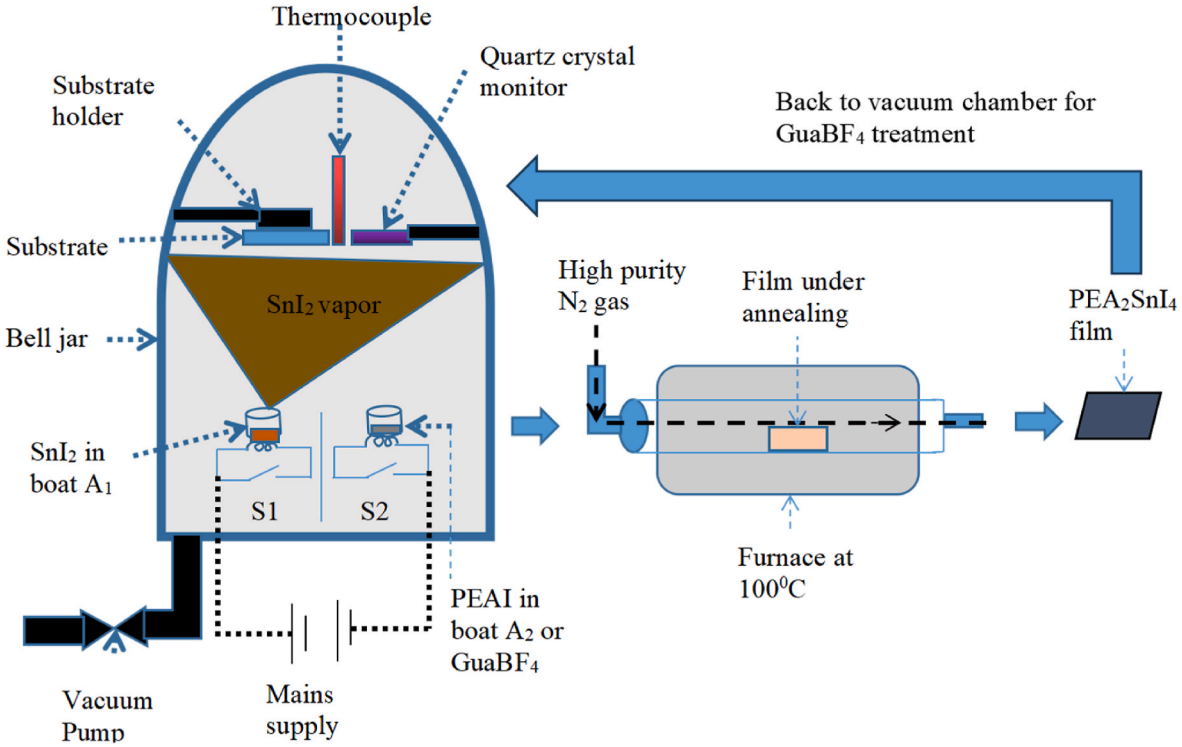

Fig. 1. Schematic showing the growth and the surface treatment process of 2D-PEA_2SnI_4 perovskite thin films using SPVD technique.

s respectively. The temperature of the substrate during the deposition process was ≈18 °C. The films were then placed inside a Lindberg Heviduty tube furnace and annealed at 100 °C for 30 min with a continuous flow of high-purity nitrogen at a rate of 5 LPM. The annealed films were quickly loaded back into the chamber and evacuated to a pressure of 2×10^{-5} mbar, and then surface treated by evaporating different thickness of $GuaBF_4$ precursor (0.5, 1 and 1.5 nm).

Film characterization: The structural properties of the films were examined by XPERT-PRO X-ray diffraction (XRD) spectrometer using Cu K-Alpha radiation source with wavelength of 1.5406 Å. 2θ was measured spanning from 5 to 50° in steps of 0.05°. The UV–Vis Cary 100 spectrometer was used to measure the optical absorption spectra of the films over the wavelength range of 300–800 nm. The Zeiss crossbeam 540 field emission scanning electron microscope (FE-SEM) was used to study the surface morphology of the films. The WITech alpha300 RAS + atomic force microscope (AFM) was used to analyze the surface topologies and to obtain the Raman spectra of the films. The RMS roughness and 3D topological images were obtained through analysis of AFM images using WITec Suite FIVE software. Measurements of Steady-state photoluminescence (PL) and time resolved photoluminescence (TRPL) spectra were performed in an ambient environment using supercontinuum pulsed laser operating at 20 MHz repetition rate (SuperK EVO, NKT Photonics) with a pulse width of ≈67 ps and an average power of ≈840 nW. The excitation light was filtered to 525 nm wavelength (SuperK VARIA, NKT Photonics, 10 nm bandwidth). A Becker & Hickl GmbH SPC-130 EM TCSPC module was used to acquire the TRPL data. The Fourier transform infrared (FTIR) spectroscopy measurements were performed using JASCO FT/IR-4X spectrometer in transmission mode.

Device fabrication and measurements: FTO/SnO_2/perovskite (with/without $GuaBF_4$)/$PC_{70}BM$/Au electron-only devices were fabricated by thermally evaporating 80 nm of SnO_2 on clean glass/FTO substrates followed by annealing at 180 °C and UV/ozone treatment for 30 min. There after 150 nm of the perovskite (with/without $GuaBF_4$) was then deposited by SPVD and annealed for 30 min followed by thermal evaporation of 50 nm of $PC_{70}BM$ and 80 nm of Gold (Au). FTO/perovskite/Au -devices were fabricated using a resistive evaporator to thermally evaporate 150 nm of the perovskite on glass/FTO substrates followed by 80 nm of Au. I-V measurements were performed using Agilent B2912A Source Measure Unit, ORIEL LCS-100 solar simulator with Air-Mass 1.5 Global (AM 1.5 G) filter and Newport 91150V silicon reference cell for calibration.

3. Results and discussion

The structural properties of the 2D-PEA_2SnI_4 perovskite thin films with and without $GuaBF_4$ surface passivation were investigated by conducting XRD measurements as shown in Fig. 2 (a). The film without $GuaBF_4$ shows a typical 2D layered perovskite with diffraction peaks associated with (00n) plane; n = 2,4,6,8,10 and12 assigned to 2θ = 5.57°, 10.91°, 16.32°, 21.82°, and 33.10° respectively. The XRD patterns of PEA2SnI_4 thin films with $GuaBF_4$ surface treatment exhibits the

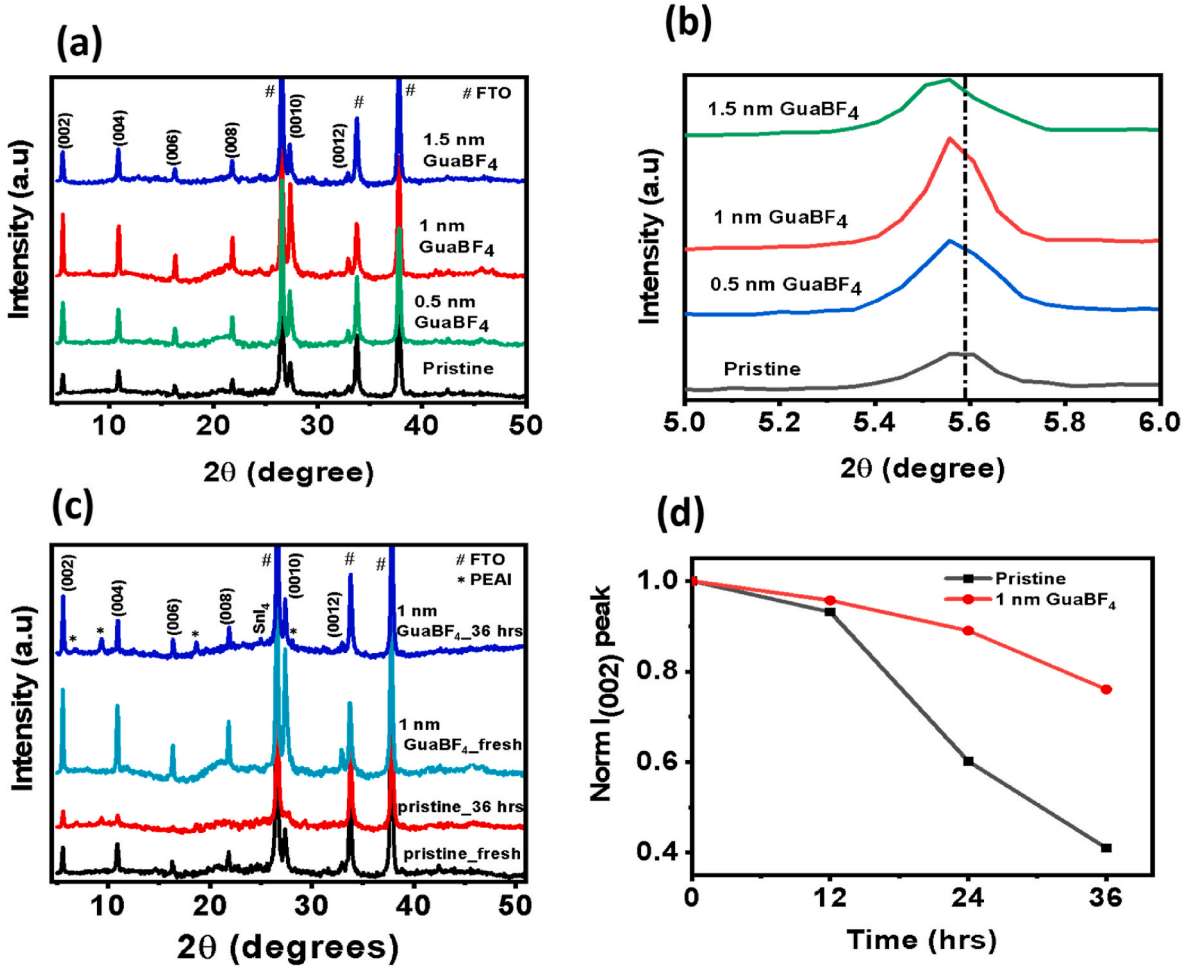

Fig. 2. (a) XRD patterns of the 2D-PEA_2SnI_4 perovskite films for pristine and varying $GuaBF_4$ thickness; (b) Comparison of the zoomed in (002) diffraction peaks; (c) XRD patterns measured on fresh films and after 36 h; (d) Variation of the normalized (002) peak intensities with time for films with and without $GuaBF_4$ stored in N_2 atmosphere at room temperature.

same diffraction peak patterns as the pristine film. However, upon surface treatment with $GuaBF_4$, the intensities of XRD peaks increased, indicating an improvement in the crystallinity of PEA_2SnI_4 perovskite films.

It can be observed that 2θ decreased from 5.57° to 5.54° as $GuaBF_4$ thickness increased from 0 to 1.5 nm. This suggests that Gua^+ cations and BF_4^- anions could be penetrating into the perovskite lattice through the grain boundaries, replacing some of the PEA^+ cations and I^- anions, respectively, at the A and X sites [36,37]. Lui et al. and Zhang et al. demonstrated that Gua^+ and BF_4^- have the ability to enter the perovskite lattice due to its similar ionic radii as A cations and X anions respectively [38,39]. This results in expansion of unit cell volume, causing shifting of 2θ peaks to lower angles. The full wave at half maximum (FWHM) decreased upon surface treatment of PEA_2SnI_4 films, with 1 nm $GuaBF_4$ exhibiting the lowest value of 0.148° as shown in Table 1. This shows that 1 nm $GuaBF_4$ surface treatment of PEA_2SnI_4 perovskite films results in the highest film quality and best crystallinity.

There is a slight shift of the peaks towards the lower 2θ angle as the thickness of $GuaBF_4$ increased as shown in Fig. 2 (b). Table 1 shows the 2θ values for (002) diffraction peaks.

The interplanar distance (d-spacing) for the PEA_2SnI_4 perovskite films were calculated using the Bragg law shown in equation (1) [40]. It can be observed in Table 1 that the (002) interlayer distance between the inorganic layers slightly increased from 15.85 to 15.92 Å due to vacuum surface treatment of PEA_2SnI_4 perovskites with $GuaBF_4$, which further confirms the possible perovskite-additive interaction.

$$n\lambda = 2dsin\theta \tag{1}$$

where λ, n, d, and θ are the wavelength, an integer, interplanar distance, and angle of diffraction respectively.

To further confirm the effect of surface passivation of PEA_2SnI_4 perovskites with $GuaBF_4$ on the crystallinity of the resulting films, the average crystallite size (D) and dislocation density (ρ) were calculated using the Williamson-Hall [41] and Williamson-Smallman [42] equations (2) and (3) respectively:

$$\beta\, cos\,\theta = \frac{k\lambda}{D} + 4\varepsilon\, sin\,\theta \tag{2}$$

$$\rho = \frac{n}{D^2} \tag{3}$$

where β, θ, λ, k, and ε are the FWHM, diffraction angle, wavelength (Cu kα = 1.5406 Å), Scherrer's constant (0.9), and micro-strain respectively, and $n = 1$ for minimum ρ.

The crystallite size of the pristine film significantly increased after the introduction $GuaBF_4$ surface passivation layer, with 1 nm of $GuaBF_4$ exhibiting the largest crystallite size. The calculated crystallite sizes (Table 1) were 39.50, 58.01, 62.78 and 53.52 nm corresponding to pristine, 0.5, 1, and 1.5 nm $GuaBF_4$ respectively. The increase in crystallite size is associated with reduction in grain boundaries and surface defects which is favourable for high optoelectronic device performance. In addition, the dislocation density decreased tremendously from 6.41 × 10^{10} to 2.54 × 10^{10} cm^{-2} upon introduction of 1 nm $GuaBF_4$ as passivation layer for PEA_2SnI_4 perovskite thin films (see Table 1). This confirms a reduction in defect density within the films treated with $GuaBF_4$, which is important for optoelectronic applications such as PeLEDs and solar cells.

Table 1
FWHM and interplanar d-spacing with the corresponding (002) 2q diffraction angle, crystallite size and dislocation density for PEA_2SnI_4 perovskite films with and without $GuaBF_4$.

$GuaBF_4$ thickness (nm)	2θ (°)	FWHM (002) peak (°)	d-spacing (Å)	Crystallite size (nm)	Dislocation density (10^{10}) cm^{-2}
0	5.57	0.188	15.85	39.50	6.409
0.5	5.56	0.172	15.86	58.01	2.972
1	5.56	0.148	15.86	62.78	2.541
1.5	5.54	0.172	15.92	53.52	3.491

Fig. 2 (c) shows the XRD patterns of PEA_2SnI_4 perovskite films with and without $GuaBF_4$ surface treatment measured on fresh films and after 36 h at room temperature. It can be observed that after 36 h, majority of the peaks describing the 2D perovskite disappeared for the pristine films while the film treated with $GuaBF_4$ retained all its characteristic 2D peaks. Furthermore, the peaks for films passivated with $GuaBF_4$ were still intense after 36 h, showing that these films exhibited relatively good crystallinity. The extra peaks appearing at 2θ = 6.85°, 9.36°, 18.68° and 28.10° are assigned to PEAI due to perovskite decomposition while the peak at 24.96° was assigned to SnI_4 due to oxidation [12,43]. It can be observed from Fig. 2 (d) that the intensity of (002) plane peak for pristine film degrades very rapidly compared to the $GuaBF_4$ surface passivated film. It is noted that the ionic radius of the BF_4^- anion (218 p.m.) is comparable to that of I^- anion (220 p.m.), hence it can replace some of the I^- ions, intercalating into the perovskite structure [44–46].

The presence of BF_4^- in perovskite lattice emerges into a very strong coordination between $F^-$and Sn^{2+} (BF_4^- donates a lone pair electron to Sn^{2+}) resulting in suppressed Sn^{2+} oxidation and enhanced stability of the PEA_2SnI_4 films [47]. In addition, BF_4^- passivates the I^- ion vacancies at the surface while Gua^+ can passivate the defects through occupation of PEA^+ vacancies or interacting with the under-coordinated I^- at the grain boundaries. Thus, the synergistic role played by Gua^+ and BF_4^- in Sn^{2+} coordination, passivation of I^- ion vacancies and other defects at the surface and grain boundaries of the perovskite, contribute to improved stability of the films.

Optical properties were further assessed on pristine and $GuaBF_4$ treated films. Fig. 3 (a) shows the UV–Vis absorption of PEA_2SnI_4 thin films for pristine and with varying thicknesses of $GuaBF_4$. All the films showed typical 2D-PEA_2SnI_4 absorption peaks at 415, 522, and 610 nm which agrees with literature [48]. The absorption of the films improved upon $GuaBF_4$ surface treatment, with a significant impact observed between 300 and 522 nm. The high absorption of the $GuaBF_4$ containing films is attributed to minimized surface defects and suppressed Sn^{2+} oxidation, resulting in high quality films.

The Tauc plot equation (4) [49] was used to estimate the bandgap (E_g) of the films, as illustrated in Fig. 3 (b).

$$\alpha h\nu = C\left(h\nu - E_g\right)^n \tag{4}$$

where α is the absorption coefficient, h represents Plancks' constant, ν is the frequency, C is a constant, and E_g is the bandgap. n is a constant which shows the nature of transition; where $n = 1/2$ for direct permitted transition, 2 for indirect permitted transition, $3/2$ for direct forbidden transition, and 3 for indirect forbidden transition.

It was observed that the pristine and $GuaBF_4$ surface passivated films had the same optical band of 1.98 eV. This suggests that $GuaBF_4$ surface treatment did not alter the band gap of PEA_2SnI_4 perovskite films, despite having a greater influence on absorption intensities. Fig. 3 (c) shows UV–Vis absorption spectra of pristine and 1 nm $GuaBF_4$ measured on fresh films and after 72 h. The film without $GuaBF_4$ surface treatment show very low absorption with no typical 2D absorption peaks after 72 h. On the other hand, $GuaBF_4$ surface treated films still show strong absorption with all its characteristic 2D peaks. This further confirms the role played by $GuaBF_4$ surface treatment on PEA_2SnI_4 films towards improving their stability. Furthermore, Fig. 3 (d) shows that the $GuaBF_4$ treated films retained over 80 % of the initial 610 nm absorption peak intensity after 72 h, while films without $GuaBF_4$ treatment retained almost 0 % of initial absorption peak intensity.

FTIR measurements were conducted to investigate the PEA_2SnI_4 perovskite-$GuaBF_4$ chemical interactions. Fig. 4 (a) shows FTIR spectra measured in transmission mode for the pristine and films surface treated with different thicknesses of $GuaBF_4$ in the 2700–4000 cm^{-1} range. The

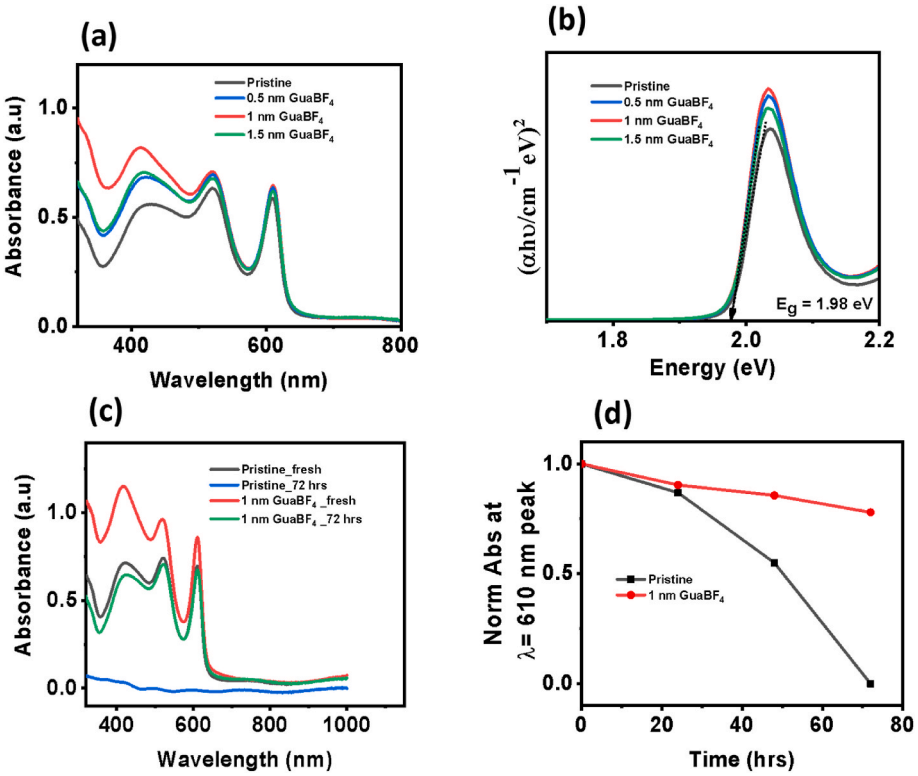

Fig. 3. (a) UV–Vis absorption spectra; (b) Tauc plot of 2D-PEA_2SnI_4 perovskite films for pristine and varying $GuaBF_4$ thickness respectively; (c) UV–Vis absorption spectra measured on fresh films and after 72 h; (d) Variation of normalized absorption peak intensities of the 610 nm peak with time for films with/without $GuaBF_4$ stored in N_2 atmosphere at room temperature.

film without $GuaBF_4$ surface treatment displays absorption peaks at ~2831.2, 2871.4, 2919.5, 3066.3, 3165.4 and 3508.3 cm^{-1}. The characteristic peaks at ~2831.2, 2871.4 and 2919.5 cm^{-1} belong to either asymmetric or symmetric C-H bond stretching or bending vibrations [37,50]. Furthermore, the peaks at ~3066.3, 3165.4 and 3508.3 cm^{-1} belong to N-H stretching vibrations [42,51]. The presence of C-H and N-H stretching or bending vibrations confirm PEA^+ as the major organic component in the PEA_2SnI_4 pristine films. It is observed that surface treatment of the films with $GuaBF_4$ does not change the FTIR spectrum but causes a change in the intensity of the peaks. Additionally, there is a slight shift in the peak positions as shown in Fig. 4 (b) in the zoomed FTIR spectrum in the 2830-2960 cm^{-1} range. There was a ~14 cm^{-1} shift from 2919.5 to 2933.5 cm^{-1} as $GuaBF_4$ thickness increased from 0 to 1.5 nm. The change in absorption peak intensities and the shift in the peak position suggest an interaction between $GuaBF_4$ and the 2D-PEA_2SnI_4 perovskite.

PL emission and TRPL decay were further measured to gain more insight on the effect of $GuaBF_4$ surface treatment on charge carrier dynamics of 2D-PEA_2SnI_4 perovskite. Fig. 4 (c) shows the normalized PL emission and absorption spectra of pristine films and 1 nm $GuaBF_4$ treated films. It can be observed that the PL emissions for the pristine and $GuaBF_4$ treated films overlap, and the emission peak (521.3 nm) agrees with the absorption onset.

This further confirms that the introduction of $GuaBF_4$ did not alter the bandgap of the 2D-PEA_2SnI_4 perovskite. In addition, both the pristine and the $GuaBF_4$ treated films display a small Stokes shift ~11.3 nm between the absorption and emission peak, which shows that the PL emission characteristics could be related to direct exciton recombination processes [37,52,53]. Fig. 4 (d) shows the PL emission spectra for pristine, 0.5, 1, and 1.5 nm $GuaBF_4$ surface treated films. The PL peak intensity is seen to increase upon $GuaBF_4$ surface treatment of PEA_2SnI_4 films, with 1 nm $GuaBF_4$ resulting in ~1.8-fold increment indicating more dominant radiative recombination.

TRPL decay lifetime measurements of PEA_2SnI_4 perovskite thin films with and without $GuaBF_4$ treatment as illustrated in Fig. 4 (e). The decay curves were fitted using a biexponential decay function in equation (5) [54]. The corresponding fitted parameters are shown in Table 2 where the average charge carrier recombination lifetimes were obtained from equation (6).

$$I(t) = B_1 \exp(-t/\tau_1) + B_2 \exp(-t/\tau_2) \quad (5)$$

$$\tau_{avg} = \left(B_1\tau_1^2 + B_2\tau_2^2\right) / \left(B_1\tau_1 + B_2\tau_2\right) \quad (6)$$

where τ_1 and τ_2 represent the fast and slow decay parts corresponding to surface trapping and radiative recombination respectively. B_1 and B_2 are the decay amplitudes. The pristine sample exhibits a fast decay lifetime component of 0.4691 ns and a slow decay lifetime of 1.360 ns resulting in an average lifetime of 0.6519 ns. On the other hand, the optimized PEA_2SnI_4 film treated with 1 nm $GuaBF_4$ displayed a fast decay lifetime of 0.5028 ns and a slow lifetime component of 1.585 ns with the corresponding average lifetime of 1.277 ns. It can be observed that the average lifetime and the slow decay lifetime of the PEA_2SnI_4 treated films increased, indicating minimized trap-assisted recombination [54]. Furthermore, the improvement in PL intensity and charge carrier lifetime shows a suppression of non-radiative recombination resulting from passivation of defect states, minimized Sn^{2+} oxidation, and improved film quality.

FE-SEM was used to assess the effect of physical vapor treatment of PEA_2SnI_4 films with $GuaBF_4$ on the micro-morphology. Fig. 5(a)–(d) shows the top view FE-SEM images of PEA_2SnI_4 perovskite thin films with and without $GuaBF_4$ treatment. It is observed in Fig. 5 (a) that the film without $GuaBF_4$ is characterised of several grain boundaries, a large number of pinholes, and non-uniform small grains making the films susceptible to non-radiative charge carrier recombination. A significant improvement in morphology is noted with a reduction in defects, enlarged grain size and more compactness upon the introduction of

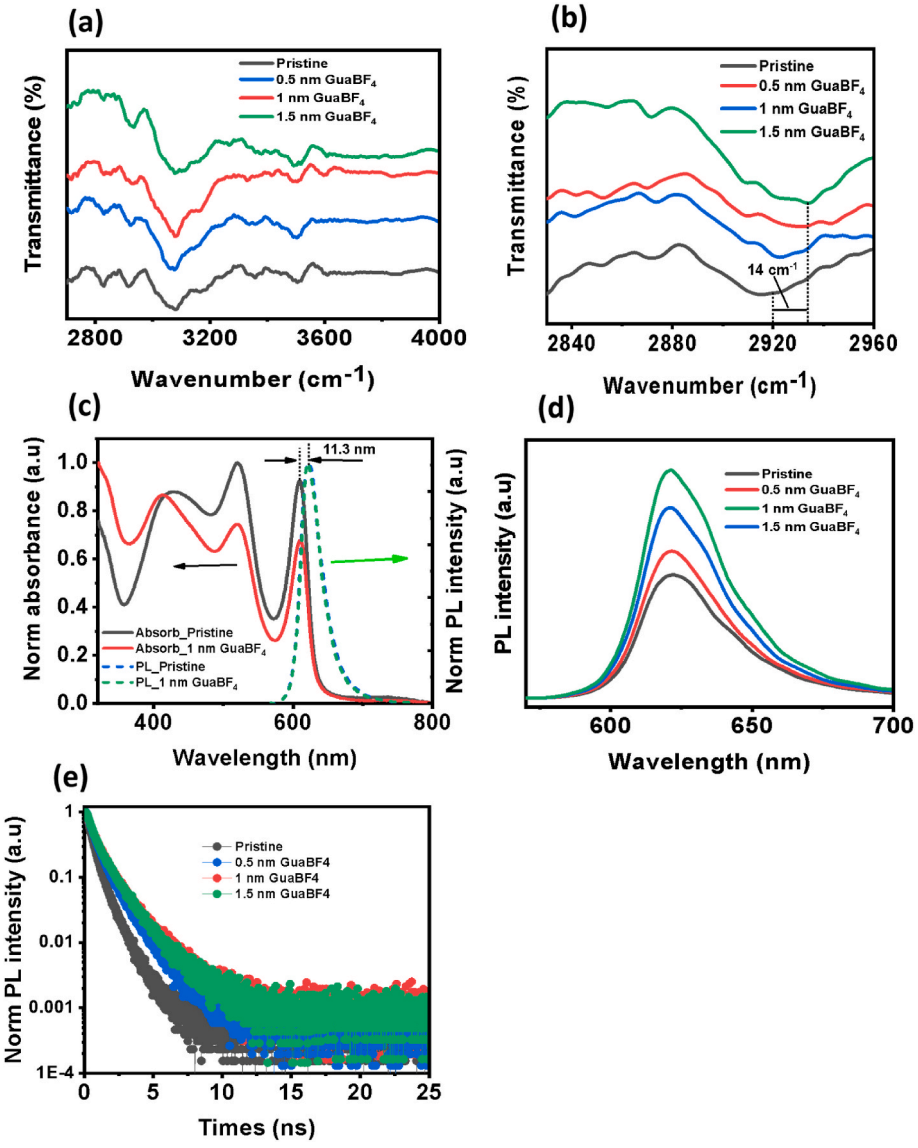

Fig. 4. (a) FTIR transmission spectrum (b) Zoomed in spectra in 2800–2960 cm^{-1} spectral range of 2D-PEA_2SnI_4 perovskite thin films prepared without and with varying thickness of $GuaBF_4$; (c)Normalized absorption and PL spectra of pristine and 1 nm $GuaBF_4$ treated film; (d) PL spectra and (e) TRPL decay spectra of 2D-PEA_2SnI_4 perovskite thin films without and with varying thickness of $GuaBF_4$.

Table 2
Fitted lifetime decay parameters of 2D-PEA_2SnI_4 perovskite thin films with varying $GuaBF_4$ thickness.

$GuaBF_4$ thickness (nm)	B_1	τ_1 (ns)	B_2	τ_2 (ns)	τ_{avg} (ns)
Pristine	1.143	0.4691	0.1018	1.360	0.6519
0.5	0.9819	0.5870	0.2328	1.567	0.9668
1	0.6224	0.5028	0.4963	1.585	1.277
1.5	0.8198	0.5403	0.3803	1.556	1.121

$GuaBF_4$ especially with the optimized thickness of 1 nm (Fig. 5 (c)). The low defect density is due to the ability of $GuaBF_4$ to passivate the grain boundaries (GBs) and defects at the grains/surface of the perovskite. The estimated average grain sizes were 238.8, 340.2, 367.5 and 348.3 nm for pristine, 0.5, 1, and 1.5 nm of $GuaBF_4$ surface treatment respectively as shown in Table 3.

Grain size enlargement can be attributed to secondary crystallization of the perovskite induced by $GuaBF_4$ as reported in halide perovskites by other research groups. Huang et al. synthesized $MAPbI_3$ perovskite by solution processing and surface passivated the resulting perovskite with $GuaBF_4$ dissolved in isopropanol [55]. The resulting perovskite film exhibited enlarged crystals compared to the pristine films brought about by secondary crystallization of the perovskite. A similar phenomenon was also reported by the same group where surface passivation of the perovskites using Gua^+ -based additive (GuaBr) resulted into optimization of secondary crystallization process, doubling the average grain sizes of the films [56].

Additionally, BF_4^- anion has been found to have a greater impact in promoting grain growth and control of crystallization in perovskites [34]. Therefore, vacuum treatment could get BF_4^- anions into the perovskite lattice through GBs, resulting in grain size enlargement and better film quality. The improved morphological properties exhibited in $GuaBF_4$ surface treated films is beneficial for improving the performance of optoelectronic devices [57]. There was, however, a slight decrease in grain size and appearance of pinholes above 1 nm $GuaBF_4$ surface treatment, attributed to excess $GuaBF_4$ [58].

Fig. 5 (e)and (f) show FE-SEM images of the films with and without $GuaBF_4$ surface treatment respectively after 72 h. The film without $GuaBF_4$ treatment showed a decrease in grain size and a large number of pinholes. Furthermore, the dark colour of the pristine perovskite film

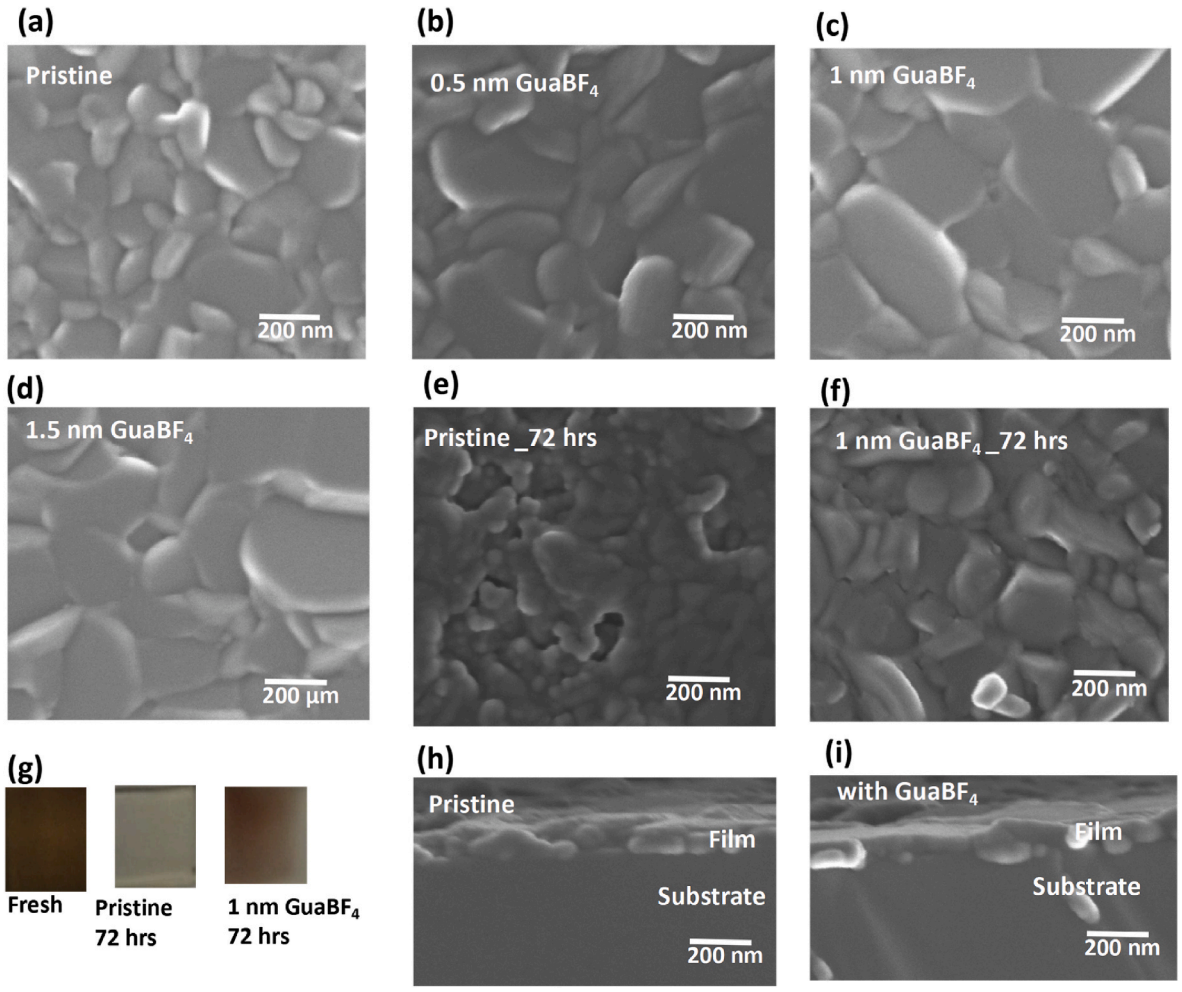

Fig. 5. (a–d) FE-SEM images of PEA_2SnI_4 perovskite thin films without and with varying thicknesses of $GuaBF_4$; (e) and (f) FE-SEM images of films with and without $GuaBF_4$ treatment respectively after 72 h; (g) photo showing colour deformation of perovskite films after 72 h of storage in N_2 atmosphere at room temperature; (h) and (i) cross-section SEM images of PEA_2SnI_4 thin films without and with $GuaBF_4$ treatment respectively.

Table 3
Average grain size for PEA_2SnI_4 perovskite films with and without $GuaBF_4$ surface treatment.

$GuaBF_4$ thickness (nm)	Average grain size (nm)
0	238.8
0.5	340.2
1	367.5
1.5	348.3

completely faded as observed in Fig. 5 (g). The deterioration of pristine film after 72 h is attributed to air and moisture permeation into the film through the grain boundaries and defects leading to oxidation of Sn^{2+} to Sn^{4+} and decomposition of perovskite. This is supported by the appearance of Sn^{4+} (SnI_4) and PEAI peaks from the XRD diffractograms in Fig. 2 (c) which are not observed in $GuaBF_4$ treated films.

Conversely, the $GuaBF_4$ surface treated film exhibited fewer pinholes (Fig. 5 (f)) with minimum fading. This was attributed to the ability of $GuaBF_4$ to passivate the grain boundaries and defects which act as air and moisture penetration centres into the film. As a result, $GuaBF_4$ surface treatment protected the films against degradation.

Figure (h) and (i) depicts the cross-section SEM images of PEA_2SnI_4 perovskite thin films without and with $GuaBF_4$ surface treatment respectively. The film without $GuaBF_4$ is composed of small grains with several grain boundaries. On the other hand, $GuaBF_4$ treated film exhibits compact and enlarged grains with fewer grain boundaries which can enhance its optoelectronic performance as a wide band gap material.

AFM characterization was used to further examine the effect of $GuaBF_4$ surface treatment on the morphology of PEA_2SnI_4 perovskite thin films. The film without $GuaBF_4$ surface treatment displayed the highest surface roughness of 37.90 nm as shown in Fig. 6 (a). A decrease in surface roughness was observed when PEA_2SnI_4 perovskite thin films were treated with $GuaBF_4$ as shown in Fig. 6(c)–(d). The measured surface roughness was 34.11, 30.72 and 33.85 nm corresponding to 0.5, 1 and 1.5 nm $GuaBF_4$ thickness. The film with 1 nm $GuaBF_4$ displayed the lowest surface roughness, demonstrating the highest film quality amongst all the films which agrees with XRD, UV–Vis and SEM results. The decrease in surface roughness demonstrates the passivation of grain boundaries and defects at the surface of the perovskite by $GuaBF_4$.

Raman spectra of 2D-PEA_2SnI_4 perovskite films for pristine and with different thicknesses of $GuaBF_4$ were further acquired in order to obtain more insight on the perovskite structure as shown in Fig. 6 (e). All films displayed the same Raman peaks located at ~65.2, 108.6 and 145.5 cm^{-1} representing mainly vibrations related to the $[SnI_6]^{4-}$ octahedron inorganic layer of PEA_2SnI_4 [37]. The Raman peaks at ~65.2, 108.6 and 145.5 cm^{-1} are assigned to B_{2g}, A_{1g}, and A_g modes and are caused by bending vibration of I-Sn-I, symmetric stretching of Sn-I, and tensile vibration of the out of plane Sn-I bond respectively [59–61]. It is observed that the film without $GuaBF_4$ treatment displayed the lowest Raman intensity for all the peaks.

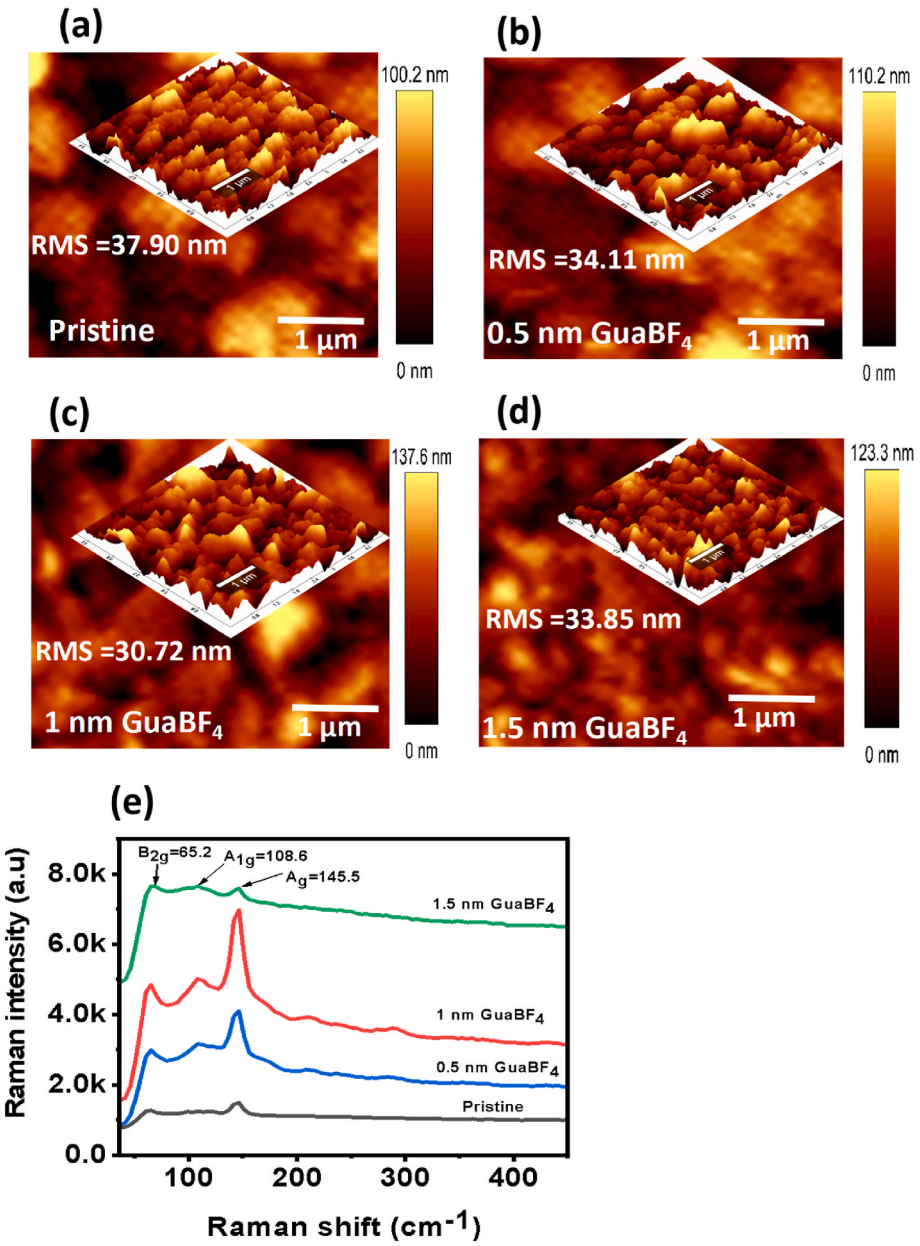

Fig. 6. (a–d) AFM images of PEA_2SnI_4 perovskite thin films without and with varying thicknesses of $GuaBF_4$. The inset represents 3D lateral images; (e) Raman spectra of pristine and $GuaBF_4$ treated PEA_2SnI_4 perovskite thin films.

The intensity of the peaks increases upon surface treatment, with 1 nm $GuaBF_4$ displaying the highest Raman intensity. This further confirms that surface treatment of PEA_2SnI_4 perovskite films with $GuaBF_4$ greatly improved the crystallinity of the films. In addition, there is no significant change in peak positions which means that $GuaBF_4$ did not change the structural phase of the perovskite which agrees with XRD results.

Electrical characterizations were further performed to assess the effect of $GuaBF_4$ surface treatment on electrical properties of the resulting films. Fig. 7 (a) illustrates the FTO/perovskite (with/without $GuaBF_4$)/Au hole-only device used for photoelectrical measurements. Fig. 7 (b) and (c) shows semi-logarithmic I-V curves for the devices based on pristine and $GuaBF_4$ treated films respectively, under dark and illumination (AM 1.5G, 100 $mWcm^{-2}$). It can be observed that all the curves are symmetric around 0 V. In addition, the current under illumination is higher than the dark current for both the pristine and $GuaBF_4$ treated-based devices, demonstrating the generation of charge carriers when the devices are illuminated. It is however noted from Fig. 7 (d) that the generated current under illumination is much higher in devices with $GuaBF_4$ treated films than the pristine devices, further confirming the role played by $GuaBF_4$ in improving the optoelectronic performance of the devices.

Fig. 7 (e) shows the FTO/SnO_2/perovskite (with/without $GuaBF_4$)/$PC_{70}BM$/Au electron-only device used for SCLC measurements. It can be observed from the double-log I-V characteristics of the electron-only device in Fig. 7 (f) that the onset voltage of the trap-filled limit region (V_{TFL}) decreased from 0.781 to 0.691 V upon treatment of PEA_2SnI_4 perovskite films with $GuaBF_4$. This demonstrated a reduction of trap defects in the $GuaBF_4$ surface treated films. The trap state defect density, N_t in the PEA_2SnI_4 (with/without $GuaBF_4$ treatment) perovskite thin films was further calculated using equation (7) from the dark I-V measurements of the electron-only device.

$$N_t = 2V_{TFL}\varepsilon_0\varepsilon_r/qd^2 \quad (7)$$

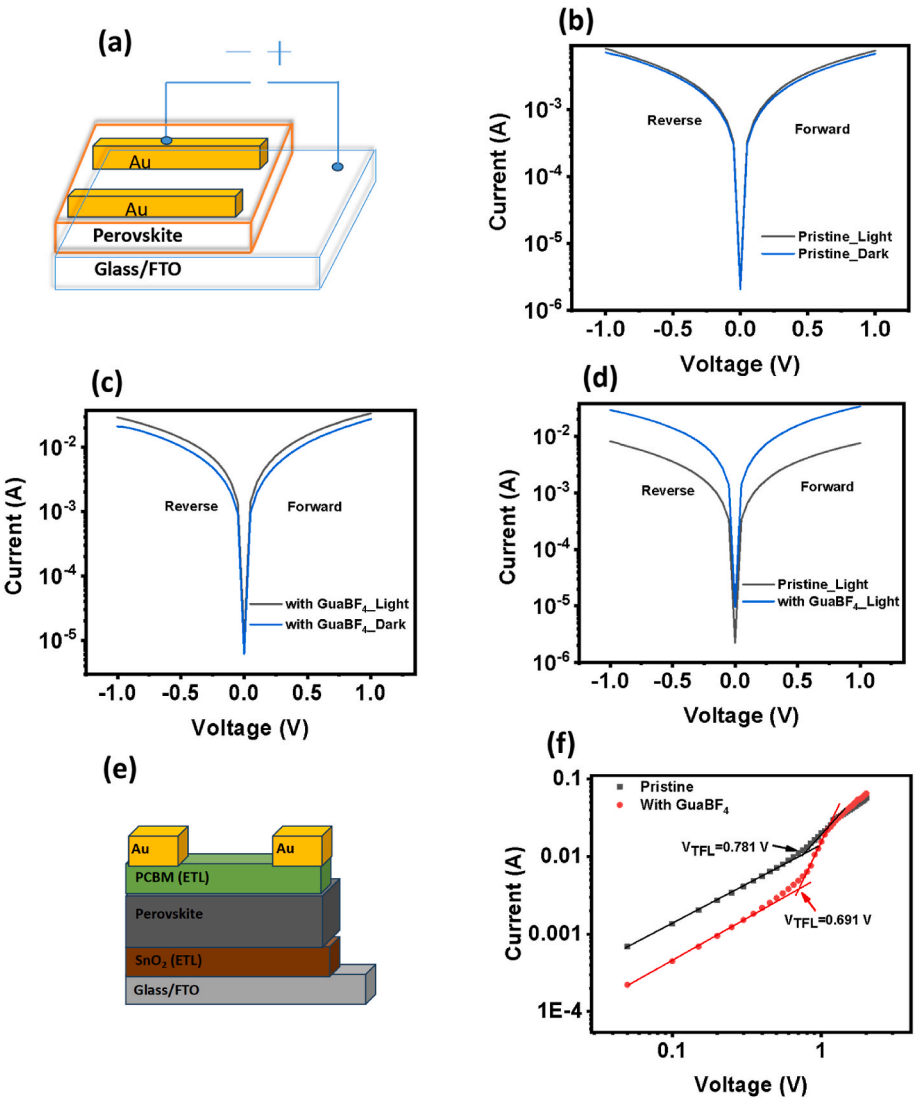

Fig. 7. (a) FTO/Perovskite (with/without $GuaBF_4$)/Au device used for photoelectrical measurements; semi-log I-V characteristics under dark and illumination for (b) pristine and (c) $GuaBF_4$ treated films; (d) comparison of semi-log I-V characteristics for pristine and $GuaBF_4$ treated films under illumination; (e) FTO/SnO_2/perovskite/$PC_{70}BM$/Au electron-only device used for SCLC measurements and (f) Dark I-V characteristics from electron-only device for pristine and $GuaBF_4$ treated film.

where ε_0 is the permittivity of free space, ε_r is the dielectric constant of the perovskite, V_{TFL} is the trap-filled limit region onset voltage, q is the elemental charge and d is the thickness of the film. It is observed that treatment of PEA_2SnI_4 films with $GuaBF_4$ decreased the defect density from 6.9×10^{15} to 6.0×10^{15} cm^{-3} attributed to defect passivation and the improved quality of the film. The reduction in the defect density agrees with PL life time measurements where a longer carrier lifetime is observed in $GuaBF_4$ treated films.

4. Conclusion

We have investigated the use of $GuaBF_4$ through a physical vapor treatment process on 2D-PEA_2SnI_4 perovskite thin films grown by SPVD. XRD results showed that treatment of PEA_2SnI_4 films with $GuaBF_4$ results into a significant improvement in crystallinity and an increase in crystallite size. SEM results revealed an improvement in morphology and an increase in grain size upon the introduction of $GuaBF_4$. The estimated average grain sizes were 238.8, 340.2, 367.5 and 348.3 nm for pristine, 0.5, 1 and 1.5 nm $GuaBF_4$ respectively. A decrease in surface roughness was observed in PEA_2SnI_4 perovskite thin films treated with $GuaBF_4$. The low surface roughness demonstrates the passivation of grain boundaries and defects at the surface of the perovskite by $GuaBF_4$ which is highly desirable for efficient optoelectronic devices. PL intensity and carrier lifetime increased by ~1.8 and 2-folds respectively due to $GuaBF_4$ surface treatment resulting from suppression of non-radiative recombination within the film. SCLC measurements revealed a reduction in the trap state density from 6.9×10^{15} to 6.0×10^{15} cm^{-3} due to $GuaBF_4$ treatment, attributed to defect passivation and the improved film quality. SEM, UV–Vis and XRD stability studies showed a significant improvement in stability of $GuaBF_4$ treated films demonstrating the role of $GuaBF_4$ in protection of the film against degradation. Our study proposes an effective strategy of producing high quality and stable solvent-free additive based 2D-Sn perovskite thin films for high performance optoelectronic applications.

CRediT authorship contribution statement

Alex Sembito: Writing – original draft, Visualization, Methodology, Investigation, Formal analysis, Data curation, Conceptualization. **Julius M. Mwabora:** Writing – review & editing, Supervision, Funding acquisition. **Francis W. Nyongesa:** Writing – review & editing, Supervision, Funding acquisition. **Mmantsae Diale:** Writing – review &

editing, Validation, Supervision, Software, Resources, Project administration, Funding acquisition, Conceptualization.

Declaration of competing interest

The authors declare the following financial interests/personal relationships which may be considered as potential competing interests: Mmantsae Diale reports financial support was provided by NRF. Alex Sembito reports financial support was provided by PASET. If there are other authors, they declare that they have no known competing financial interests or personal relationships that could have appeared to influence the work reported in this paper.

Acknowledgements

The authors thank Partnership for Skills in Applied Sciences, Engineering and Technology (PASET)-RSIF and South African Research Chair (SARChI), UID 115463 for funding. We also acknowledge Michael Lovemore for PL and TRPL measurements. University of Nairobi (UoN) partnership with University of Pretoria is acknowledged for providing access to laboratories for synthesis and characterization of the films.

Data availability

Data will be made available on request.

References

[1] Y.J. Heo, H.J. Jang, J.-H. Lee, S.B. Jo, S. Kim, D.H. Ho, S.J. Kwon, K. Kim, I. Jeon, J.-M. Myoung, J.Y. Lee, J.-W. Lee, J.H. Cho, Enhancing performance and stability of tin halide perovskite light emitting diodes via coordination engineering of lewis acid–base adducts, Adv. Funct. Mater. 31 (2021) 2106974, https://doi.org/10.1002/adfm.202106974.

[2] L. Gao, L.N. Quan, F.P. García de Arquer, Y. Zhao, R. Munir, A. Proppe, R. Quintero-Bermudez, C. Zou, Z. Yang, M.I. Saidaminov, O. Voznyy, S. Kinge, Z. Lu, S.O. Kelley, A. Amassian, J. Tang, E.H. Sargent, Efficient near-infrared light-emitting diodes based on quantum dots in layered perovskite, Nat. Photonics 14 (2020) 227–233, https://doi.org/10.1038/s41566-019-0577-1.

[3] M.-H. Li, H.-H. Yeh, Y.-H. Chiang, U.-S. Jeng, C.-J. Su, H.-W. Shiu, Y.-J. Hsu, N. Kosugi, T. Ohigashi, Y.-A. Chen, P.-S. Shen, P. Chen, T.-F. Guo, Highly efficient 2D/3D hybrid perovskite solar cells via low-pressure vapor-assisted solution process, Adv. Mater. 30 (2018) 1801401, https://doi.org/10.1002/adma.201801401.

[4] E. Shi, Y. Gao, B.P. Finkenauer, Akriti, A.H. Coffey, L. Dou, Two-dimensional halide perovskite nanomaterials and heterostructures, Chem. Soc. Rev. 47 (2018) 6046–6072, https://doi.org/10.1039/C7CS00886D.

[5] J.S. Manser, J.A. Christians, P.V. Kamat, Intriguing optoelectronic properties of metal halide perovskites, Chem. Rev. 116 (2016) 12956–13008, https://doi.org/10.1021/acs.chemrev.6b00136.

[6] L.N. Quan, M. Yuan, R. Comin, O. Voznyy, E.M. Beauregard, S. Hoogland, A. Buin, A.R. Kirmani, K. Zhao, A. Amassian, D.H. Kim, E.H. Sargent, Ligand-stabilized reduced-dimensionality perovskites, J. Am. Chem. Soc. 138 (2016) 2649–2655, https://doi.org/10.1021/jacs.5b11740.

[7] Y. Lin, Y. Bai, Y. Fang, Q. Wang, Y. Deng, J. Huang, Suppressed ion migration in low-dimensional perovskites, ACS Energy Lett. 2 (2017) 1571–1572, https://doi.org/10.1021/acsenergylett.7b00442.

[8] T. Matsushima, S. Terakawa, M.R. Leyden, T. Fujihara, C. Qin, C. Adachi, Toward air-stable field-effect transistors with a tin iodide-based hybrid perovskite semiconductor, J. Appl. Phys. 125 (2019) 235501, https://doi.org/10.1063/1.5097433.

[9] Y. Chen, Y. Sun, J. Peng, J. Tang, K. Zheng, Z. Liang, 2D ruddlesden–popper perovskites for optoelectronics, Adv. Mater. 30 (2018) 1703487, https://doi.org/10.1002/adma.201703487.

[10] Y. Reo, H. Zhu, J.-Y. Go, K. In Shim, A. Liu, T. Zou, H. Jung, H. Kim, J. Hong, J. W. Han, Y.-Y. Noh, Effect of monovalent metal iodide additives on the optoelectric properties of two-dimensional Sn-based perovskite films, Chem. Mater. 33 (2021) 2498–2505, https://doi.org/10.1021/acs.chemmater.0c04786.

[11] Y. Gao, Z. Wei, P. Yoo, E. Shi, M. Zeller, C. Zhu, P. Liao, L. Dou, Highly stable lead-free perovskite field-effect transistors incorporating linear π-conjugated organic ligands, J. Am. Chem. Soc. 141 (2019) 15577–15585, https://doi.org/10.1021/jacs.9b06276.

[12] Y. Ju, X. Wu, S. Huang, G. Dai, T. Song, H. Zhong, The evolution of photoluminescence properties of PEA2SnI4 upon oxygen exposure: insight into concentration effects, Adv. Funct. Mater. 32 (2022) 2108296, https://doi.org/10.1002/adfm.202108296.

[13] L. Lanzetta, T. Webb, N. Zibouche, X. Liang, D. Ding, G. Min, R.J.E. Westbrook, B. Gaggio, T.J. Macdonald, M.S. Islam, S.A. Haque, Degradation mechanism of hybrid tin-based perovskite solar cells and the critical role of tin (IV) iodide, Nat. Commun. 12 (2021) 2853, https://doi.org/10.1038/s41467-021-22864-z.

[14] M. Awais, R.L. Kirsch, V. Yeddu, M.I. Saidaminov, Tin halide perovskites going forward: frost diagrams offer hints, ACS Mater. Lett. 3 (2021) 299–307, https://doi.org/10.1021/acsmaterialslett.0c00571.

[15] Q. Tai, X. Guo, G. Tang, P. You, T.-W. Ng, D. Shen, J. Cao, C.-K. Liu, N. Wang, Y. Zhu, C.-S. Lee, F. Yan, Antioxidant grain passivation for air-stable tin-based perovskite solar cells, Angew. Chem. 131 (2019) 816–820, https://doi.org/10.1002/ange.201811539.

[16] H. Liang, F. Yuan, A. Johnston, C. Gao, H. Choubisa, Y. Gao, Y.-K. Wang, L. K. Sagar, B. Sun, P. Li, G. Bappi, B. Chen, J. Li, Y. Wang, Y. Dong, D. Ma, Y. Gao, Y. Liu, M. Yuan, M.I. Saidaminov, S. Hoogland, Z.-H. Lu, E.H. Sargent, High color purity lead-free perovskite light-emitting diodes via Sn stabilization, Adv. Sci. 7 (2020) 1903213, https://doi.org/10.1002/advs.201903213.

[17] L. Ma, F. Hao, C.C. Stoumpos, B.T. Phelan, M.R. Wasielewski, M.G. Kanatzidis, Carrier diffusion lengths of over 500 nm in lead-free perovskite CH3NH3SnI3 films, J. Am. Chem. Soc. 138 (2016) 14750–14755, https://doi.org/10.1021/jacs.6b09257.

[18] F. Gu, S. Ye, Z. Zhao, H. Rao, Z. Liu, Z. Bian, C. Huang, Improving performance of lead-free formamidinium tin triiodide perovskite solar cells by tin source purification, Sol. RRL 2 (2018) 1800136, https://doi.org/10.1002/solr.201800136.

[19] I.-H. Chao, Y.-T. Yang, M.-H. Yu, C.-H. Chen, C.-H. Liao, B.-H. Lin, I.-C. Ni, W.-C. Chen, A.W.Y. Ho-Baillie, C.-C. Chueh, Performance enhancement of lead-free 2D tin halide perovskite transistors by surface passivation and its impact on non-volatile photomemory characteristics, Small 19 (2023) 2207734, https://doi.org/10.1002/smll.202207734.

[20] C. Wang, S. Cui, Y. Ju, Y. Chen, S. Chang, H. Zhong, Color-stable two-dimensional tin-based perovskite light-emitting diodes: passivation effects of diphenylphosphine oxide derivatives, Adv. Funct. Mater. 33 (2023) 2301304, https://doi.org/10.1002/adfm.202301304.

[21] C. Gao, Y. Jiang, C. Sun, J. Han, T. He, Y. Huang, K. Yao, M. Han, X. Wang, Y. Wang, Y. Gao, Y. Liu, M. Yuan, H. Liang, Multifunctional naphthol sulfonic salt incorporated in lead-free 2D tin halide perovskite for red light-emitting diodes, ACS Photonics 7 (2020) 1915–1922, https://doi.org/10.1021/acsphotonics.0c00497.

[22] F. Yuan, X. Zheng, A. Johnston, Y.-K. Wang, C. Zhou, Y. Dong, B. Chen, H. Chen, J. Z. Fan, G. Sharma, P. Li, Y. Gao, O. Voznyy, H.-T. Kung, Z.-H. Lu, O.M. Bakr, E. H. Sargent, Color-pure red light-emitting diodes based on two-dimensional lead-free perovskites, Sci. Adv. 6 (2020) eabb0253, https://doi.org/10.1126/sciadv.abb0253.

[23] Z. Wang, F. Wang, B. Zhao, S. Qu, T. Hayat, A. Alsaedi, L. Sui, K. Yuan, J. Zhang, Z. Wei, Z. Tan, Efficient two-dimensional tin halide perovskite light-emitting diodes via a spacer cation substitution strategy, J. Phys. Chem. Lett. 11 (2020) 1120–1127, https://doi.org/10.1021/acs.jpclett.9b03565.

[24] M. Yu, X. Mei, T. Qin, R. Zhuang, Y. Hua, X. Zhang, Modulating phase distribution and passivating surface defects of quasi-2D perovskites via potassium tetrafluoroborate for light-emitting diodes, Chem. Eng. J. 450 (2022) 138021, https://doi.org/10.1016/j.cej.2022.138021.

[25] N.D. Marco, H. Zhou, Q. Chen, P. Sun, Z. Liu, L. Meng, E.-P. Yao, Y. Liu, A. Schiffer, Y. Yang, Guanidinium: a route to enhanced carrier lifetime and open-circuit voltage in hybrid perovskite solar cells, Nano Lett. 16 (2016) 1009–1016, https://doi.org/10.1021/acs.nanolett.5b04060.

[26] J. Tong, Z. Song, D.H. Kim, X. Chen, C. Chen, A.F. Palmstrom, P.F. Ndione, M. O. Reese, S.P. Dunfield, O.G. Reid, J. Liu, F. Zhang, S.P. Harvey, Z. Li, S. T. Christensen, G. Teeter, D. Zhao, M.M. Al-Jassim, M.F.A.M. van Hest, M.C. Beard, S.E. Shaheen, J.J. Berry, Y. Yan, K. Zhu, Carrier lifetimes of >1 μs in Sn-Pb perovskites enable efficient all-perovskite tandem solar cells, Science 364 (2019) 475–479, https://doi.org/10.1126/science.aav7911.

[27] N. Cheng, W. Li, M. Zhang, H. Wu, S. Sun, Z. Zhao, Z. Xiao, Z. Sun, W. Zi, L. Fang, Enhance the performance and stability of methylammonium lead iodide perovskite solar cells with guanidinium thiocyanate additive, Curr. Appl. Phys. 19 (2018), https://doi.org/10.1016/j.cap.2018.10.020.

[28] R.J. Stoddard, A. Rajagopal, R.L. Palmer, I.L. Braly, A.K.-Y. Jen, H.W. Hillhouse, Enhancing defect tolerance and phase stability of high-bandgap perovskites via guanidinium alloying, ACS Energy Lett. 3 (2018) 1261–1268, https://doi.org/10.1021/acsenergylett.8b00576.

[29] D.J. Kubicki, D. Prochowicz, A. Hofstetter, M. Saski, P. Yadav, D. Bi, N. Pellet, J. Lewiński, S.M. Zakeeruddin, M. Grätzel, L. Emsley, Formation of stable mixed guanidinium–methylammonium phases with exceptionally long carrier lifetimes for high-efficiency lead iodide-based perovskite photovoltaics, J. Am. Chem. Soc. 140 (2018) 3345–3351, https://doi.org/10.1021/jacs.7b12860.

[30] W. Zhang, J. Xiong, J. Li, W.A. Daoud, Guanidinium induced phase separated perovskite layer for efficient and highly stable solar cells, J. Mater. Chem. A 7 (2019) 9486–9496, https://doi.org/10.1039/C9TA01893J.

[31] M. Chen, M.A. Kamarudin, A.K. Baranwal, G. Kapil, T.S. Ripolles, K. Nishimura, D. Hirotani, S.R. Sahamir, Z. Zhang, C. Ding, Y. Sanehira, J. Bisquert, Q. Shen, S. Hayase, High-efficiency lead-free wide band gap perovskite solar cells via guanidinium bromide incorporation, ACS Appl. Energy Mater. 4 (2021) 5615–5624, https://doi.org/10.1021/acsaem.1c00413.

[32] S. Wu, Z. Li, J. Zhang, T. Liu, Z. Zhu, A.K.-Y. Jen, Efficient large guanidinium mixed perovskite solar cells with enhanced photovoltage and low energy losses, Chem. Commun. 55 (2019) 4315–4318, https://doi.org/10.1039/C9CC00016J.

[33] X. Hou, Y. Hu, H. Liu, A. Mei, X. Li, M. Duan, G. Zhang, Y. Rong, H. Han, Effect of guanidinium on mesoscopic perovskite solar cells, J. Mater. Chem. A 5 (2017) 73–78, https://doi.org/10.1039/c6ta08418d.

[34] H. Kim, J.W. Lee, G.R. Han, S.K. Kim, J.H. Oh, Synergistic effects of cation and anion in an ionic imidazolium tetrafluoroborate additive for improving the efficiency and stability of half-mixed Pb-Sn perovskite solar cells, Adv. Funct. Mater. 31 (2021) 2008801, https://doi.org/10.1002/adfm.202008801.
[35] J. Ávila, C. Momblona, P.P. Boix, M. Sessolo, H.J. Bolink, Vapor-deposited perovskites: the route to high-performance solar cell production? Joule 1 (2017) 431–442, https://doi.org/10.1016/j.joule.2017.07.014.
[36] Y. Wu, Q. Zhang, L. Fan, C. Liu, M. Wu, D. Wang, T. Zhang, Surface reconstruction-induced efficient CsPbI2Br perovskite solar cell using phenylethylammonium iodide, ACS Appl. Energy Mater. 4 (2021) 5583–5589, https://doi.org/10.1021/acsaem.1c00295.
[37] E. Ren, C. Zhang, F. Wang, J. Kong, L. Li, J. Chen, J. Xu, Y. zhang, Synthesis of Cs+-Tuned (PEA)2PbI4 perovskite thin films by one-step spin coating, ECS J. Solid State Sci. Technol. 12 (2023) 026003, https://doi.org/10.1149/2162-8777/acbb26.
[38] X. Liu, J. Wu, Y. Yang, D. Wang, G. Li, X. Wang, W. Sun, Y. Wei, Y. Huang, M. Huang, L. Fan, Z. Lan, J. Lin, K.-C. Ho, Additive engineering by bifunctional guanidine sulfamate for highly efficient and stable perovskites solar cells, Small 16 (2020) 2004877, https://doi.org/10.1002/smll.202004877.
[39] J. Zhang, S. Wu, T. Liu, Z. Zhu, A.K.-Y. Jen, Boosting photovoltaic performance for lead halide perovskites solar cells with BF4− anion substitutions, Adv. Funct. Mater. 29 (2019) 1808833, https://doi.org/10.1002/adfm.201808833.
[40] C.G. Pope, X-ray diffraction and the Bragg equation, J. Chem. Educ. 74 (1997) 129, https://doi.org/10.1021/ed074p129.
[41] V.S. Vinila, J. Isac, Synthesis and structural studies of superconducting perovskite GdBa2Ca3Cu4O10.5+δ nanosystems, in: S. Thomas, N. Kalarikkal, A.R. Abraham (Eds.), Des. Fabr. Charact. Multifunct. Nanomater., Elsevier, 2022, pp. 319–341, https://doi.org/10.1016/B978-0-12-820558-7.00022-4.
[42] M.M. Abdelhamied, Y. Gao, X. Li, W. Liu, Boosting the photoluminescence of 2D organic–inorganic perovskite films by mixing with polymers, Appl. Phys. A 128 (2021) 57, https://doi.org/10.1007/s00339-021-05189-y.
[43] J. Qing, C. Kuang, H. Wang, Y. Wang, X.-K. Liu, S. Bai, M. Li, T.C. Sum, Z. Hu, W. Zhang, F. Gao, High-quality ruddlesden-popper perovskite films based on in situ formed organic spacer cations, Adv. Mater. Deerfield Beach Fla 31 (2019) e1904243, https://doi.org/10.1002/adma.201904243.
[44] J. Chen, Y. Rong, A. Mei, Y. Xiong, T. Liu, Y. Sheng, P. Jiang, L. Hong, Y. Guan, X. Zhu, X. Hou, M. Duan, J. Zhao, X. Li, H. Han, Hole-Conductor-free fully printable mesoscopic solar cell with mixed-anion perovskite CH3NH3PbI(3−x)(BF4)x, Adv. Energy Mater. 6 (2016) 1502009, https://doi.org/10.1002/aenm.201502009.
[45] Y. Sheng, A. Mei, S. Liu, M. Duan, P. Jiang, C. Tian, Y. Xiong, Y. Rong, H. Han, Y. Hu, Mixed (5-AVA)xMA1−xPbI3−y(BF4)y perovskites enhance the photovoltaic performance of hole-conductor-free printable mesoscopic solar cells, J. Mater. Chem. A 6 (2018) 2360–2364, https://doi.org/10.1039/C7TA09604F.
[46] S. Nagane, S. Ogale, CH3NH3Pb(BF4)3 and (C4H9NH3)2Pb(BF4)4 family of 3D and 2D perovskites without and with iodide and bromide ions substitution, J. Phys. Chem. Lett. 7 (2016) 4757–4762, https://doi.org/10.1021/acs.jpclett.6b02121.
[47] H. Li, Y. Xu, S. Ramakrishnan, Y. Zhang, M. Cotlet, T.L. Xu, Q. Yu, Pseudo-halide anion engineering for efficient quasi-2D Ruddlesden-Popper tin perovskite solar cells, Cell Rep, Phys. Sci. 3 (2022) 101060, https://doi.org/10.1016/j.xcrp.2022.101060.
[48] K.-R. Yun, T.-J. Lee, S.-K. Kim, J.-H. Kim, T.-Y. Seong, Fast and highly sensitive photodetectors based on Pb-free Sn-based perovskite with additive engineering, Adv. Opt. Mater. 11 (2023) 2201974, https://doi.org/10.1002/adom.202201974.
[49] E.A. Davis, N.F. Mott, Conduction in non-crystalline systems V. Conductivity, optical absorption and photoconductivity in amorphous semiconductors, Philos. Mag. J. Theor. Exp. Appl. Phys. 22 (1970) 903–922, https://doi.org/10.1080/14786437008221061.
[50] J. Li, R. Yang, L. Que, Y. Wang, F. Wang, J. Wu, S. Li, Optimization of anti-solvent engineering toward high performance perovskite solar cells, J. Mater. Res. 34 (2019) 2416–2424, https://doi.org/10.1557/jmr.2019.122.
[51] S.S. Chigari, V C c, V C c, Sf M, Vk B, R A v, Ultrasonic radiation assisted synthesis of (CH3NH3)2CuCl4, CH3NH3PbCl3, and CH3NH3SnCl3 perovskites for energy application, J. Hazard. Mater. Adv. 12 (2023) 100368, https://doi.org/10.1016/j.hazadv.2023.100368.
[52] H. Huang, A.S. Susha, S.V. Kershaw, T.F. Hung, A.L. Rogach, Control of emission color of high quantum yield CH3NH3PbBr3 perovskite quantum dots by precipitation temperature, Adv. Sci. 2 (2015) 1500194, https://doi.org/10.1002/advs.201500194.
[53] C. Zhang, C. Wang, J. Chen, F. Wang, J. Kong, L. Li, H. Dong, Y. Sun, X. Peng, J. Xu, Synthesis of perovskite nanocrystal films with a high luminous efficiency and an enhanced stability, Ceram. Int. 47 (2021) 33788–33797, https://doi.org/10.1016/j.ceramint.2021.08.290.
[54] Y. Song, W. Liu, C. Fang, D. Li, P. Lu, Enhanced optoelectronic performance of 2D organic-inorganic hybrid perovskite through light-illumination, Opt Express 27 (2019) 30618–30628, https://doi.org/10.1364/OE.27.030618.
[55] B. Huang, X. Xia, X. Wang, F. Li, Surface treatment enabled by functional guanidinium tetrafluoroborate achieving high-performance inverted perovskite solar cells, Sol. Energy Mater. Sol. Cells 240 (2022) 111682, https://doi.org/10.1016/j.solmat.2022.111682.
[56] Y. Huang, Y. Li, E.L. Lim, T. Kong, Y. Zhang, J. Song, A. Hagfeldt, D. Bi, Stable layered 2D perovskite solar cells with an efficiency of over 19% via multifunctional interfacial engineering, J. Am. Chem. Soc. 143 (2021) 3911–3917, https://doi.org/10.1021/jacs.0c13087.
[57] Z.-G. Ma, Y. Shen, K. Zhang, L.-X. Cao, H. Ren, W.-S. Chen, H.-X. Wei, Y.-Q. Li, S. Kera, J.-X. Tang, Regulated crystallization with minimized degradation for pure-red lead-free perovskite light-emitting diodes, J. Mater. Chem. C 11 (2023) 9916–9924, https://doi.org/10.1039/D3TC01743E.
[58] S. Wang, Z. Ma, B. Liu, W. Wu, Y. Zhu, R. Ma, C. Wang, High-performance perovskite solar cells with large grain-size obtained by using the lewis acid-base adduct of thiourea, Sol. RRL 2 (2018), https://doi.org/10.1002/solr.201800034.
[59] G.K. Kasi, N.R. Dollahon, T.S. Ahmadi, Fabrication and characterization of solid PbI_2 nanocrystals, J. Phys. Appl. Phys. 40 (2007) 1778–1783, https://doi.org/10.1088/0022-3727/40/6/026.
[60] B. Dhanabalan, Y.-C. Leng, G. Biffi, M.-L. Lin, P.-H. Tan, I. Infante, L. Manna, M. P. Arciniegas, R. Krahne, Directional anisotropy of the vibrational modes in 2D-layered perovskites, ACS Nano 14 (2020) 4689–4697, https://doi.org/10.1021/acsnano.0c00435.
[61] S.P. Senanayak, B. Yang, T.H. Thomas, N. Giesbrecht, W. Huang, E. Gann, B. Nair, K. Goedel, S. Guha, X. Moya, C.R. McNeill, P. Docampo, A. Sadhanala, R.H. Friend, H. Sirringhaus, Understanding charge transport in lead iodide perovskite thin-film field-effect transistors, Sci. Adv. 3 (2017) e1601935, https://doi.org/10.1126/sciadv.1601935.